Materials Science in Semiconductor Processing 149 (2022) 106889

Contents lists available at ScienceDirect

Materials Science in Semiconductor Processing

journal homepage: www.elsevier.com/locate/mssp

Revealing plasmon-phonon interaction in nanocrystalline $MgFe_2O_4$ spinels by far-infrared reflection spectroscopy

Novica Paunović [a,*], Zorana Dohčević-Mitrović [a,**], Dejan M. Djokić [a], Sonja Aškrabić [a], Saša Lazović [a], Ann Rose Abraham [b], Balakrishnan Raneesh [c], Nandakumar Kalarikkal [d,e], Sabu Thomas [e,f]

[a] Institute of Physics Belgrade, University of Belgrade, Pregrevica 118, 11080, Belgrade, Serbia
[b] Department of Physics, Sacred Heart College, Kochi, Kerala, 682013, India
[c] Department of Physics, Catholicate College, Pathanamthitta, Kerala, 689645, India
[d] School of Pure and Applied Physics, Mahatma Gandhi University, Kottayam, Kerala, 686560, India
[e] International & Inter University Centre for Nanoscience and Nanotechnology, Mahatma Gandhi University, Kottayam, Kerala, 686560, India
[f] School of Energy Materials, Mahatma Gandhi University, Kottayam, Kerala, 686560, India

ARTICLE INFO

Keywords:
Magnesium ferrite
Inverse spinels
Infrared spectroscopy
Plasmon-phonon interaction

ABSTRACT

Room-temperature far-infrared reflectivity spectra of nanocrystalline, partially inverse $MgFe_2O_4$ were investigated. $MgFe_2O_4$ samples were prepared by sol-gel method and sintered at three different temperatures (400, 600 and 800 °C). Raman spectroscopy was employed to estimate the degree of inversion in the sintered samples. The degree of inversion was found to increase from 0.52 to 0.74 as the sintering temperature increased from 400 °C to 800 °C. The reflectivity spectra, besides the four infrared modes characteristic for spinels (ν_1, ν_2, ν_3, ν_4), revealed the presence of free carriers. Plasmon-longitudinal optical (LO) phonon interaction was analyzed using factorized coupled and decoupled plasmon-phonon models, combined with the Bruggeman effective medium approximation. From these models it was obtained that the ν_1 and ν_3 phonon modes are more strongly coupled with plasmons than the ν_2 mode. A potential mechanism of plasmon-phonon interaction in inverse $MgFe_2O_4$ spinel has been discussed.

1. Introduction

Magnesium ferrite ($MgFe_2O_4$) belongs to the family of spinel ferrites, a very important group of magnetic spinel oxides with a wide range of applications. It is a soft magnetic n-type semiconducting material which received strong attention due its vast uses such as magnetic applications [1,2], catalyst [3,4], metal ion removal [5], water purification [6], water and CO_2 splitting [7,8] or sensors [9]. It is considered as promising candidate for biomedical applications such as hyperthermia and cancer treatment [10–12], targeted drug delivery [13] or magnetic resonance imaging [14]. In recent years $MgFe_2O_4$ has been considered as an anode material for lithium-ion batteries [15–17]. Many properties of $MgFe_2O_4$ depend on the microstructure, grain size and porosity, or preparative methods. Preparation of $MgFe_2O_4$ in nanocrystalline form offers a way to change and tune its optical, electronic, magnetic and other properties [18–20].

Spinel oxides have a general formula AB_2O_4 and belong to the $Fd\bar{3}m$ (O_h^7, No. 227) space group. In normal spinels, A cations occupy only the tetrahedral sites, whereas B cations occupy only the octahedral sites (Fig. 1). In inverse spinels, A cations and half of B cations occupy the octahedral sites while the tetrahedral sites are occupied by the other half of the B cations, which can be represented as $B[AB]O_4$. The intermediate configurations are partially inverse spinels and the structural formula can be written as $(A_{1-\delta}\ B_\delta)_{tetra}[A_\delta B_{2-\delta}]_{octa}O_4$, where δ represents the degree of inversion, which in extreme cases of normal and completely inverse spinels has values $\delta = 0$ and $\delta = 1$, respectively. $MgFe_2O_4$ is a partially inverse spinel for which the degree of inversion δ depends on the synthesis method and thermal treatment. The crystallite size also presents an important factor for adjusting the degree of inversion and fine-tuning of $MgFe_2O_4$ properties.

Far infrared (IR) reflection spectroscopy is a powerful technique

* Corresponding author.
** Corresponding author.
E-mail addresses: paun@ipb.ac.rs (N. Paunović), zordoh@ipb.ac.rs (Z. Dohčević-Mitrović).

https://doi.org/10.1016/j.mssp.2022.106889
Received 17 March 2022; Received in revised form 2 June 2022; Accepted 8 June 2022
Available online 15 June 2022

which is often used for investigation of crystal structure, phonon and dielectric properties, phase composition, plasmon-fonon interaction, etc., in various types of materials such as oxides, semiconductors, ceramics and many others (e.g., Refs. [21–26]). IR spectroscopy is also commonly used to study normal and inverse spinels. Group theory analysis predicts four active IR modes for spinel structures. Experimental spectra of spinels show at least two strong modes, which, after works of Waldron [27], Hafner [28], and White and DeAngelis [29], are mostly accepted to originate from stretching vibrations of the tetrahedral (octahedral) groups, although it has been argued by Preudhomme and Tarte [30–33] that the actual behavior might be more complex than this. In many spinels, a third, and sometimes a weak forth mode is present at lower frequencies [28,29,32,34–36]. The exact nature of these two modes is not completely clarified yet, but is generally considered that these modes originate from complex vibrations involving both tetrahedral and octahedral groups [27,32,33,35–37]. In most reports, the IR spectra of spinels are presented as transmission or absorption spectra and the IR modes are simply analyzed by the peaks positions (e.g., Refs. [27–30,32,33,35,38–44]). On the other hand, the IR reflectivity spectra of spinels are significantly less often represented in literature (e.g., Refs. [34,36,39,45–49]). To the best of our knowledge, no infrared reflectivity spectra of $MgFe_2O_4$ has been reported. The reflectivity spectra can be more quantitatively analyzed by using an appropriate model for obtaining the values of phonon TO/LO frequencies and dampings. Furthermore, the advantages of reflectivity spectra over the transmittance ones lies in the fact that not only phonon modes but also plasmons and mutual interaction between phonons and plasmons can be analyzed. The knowledge of plasmon-phonon interaction can be important in characterizing transport and optical properties of spinels. Up to date, no infrared reflectivity study of plasmon-LO phonon interaction in $MgFe_2O_4$ has been carried out.

In the present study we have focused on the analysis of far-IR reflectivity spectra of nanocrystalline $MgFe_2O_4$ samples sintered at different temperatures and of varying degrees of inversion. The reflectivity spectra of the samples showed a clear presence of free carriers contribution. The influence of free carriers on the phonon spectra was analyzed employing two different factorized dielectric-function models, from which the coupled (decoupled) LO-phonon modes frequencies and dampings were obtained. Such analysis of reflectivity spectra paves the way for better understanding of the carrier-lattice coupling in inverse nanocrystalline $MgFe_2O_4$.

2. Experimental

Magnesium ferrite ($MgFe_2O_4$) nanocrystalline samples were prepared by sol-gel method and by sintering in air at different temperatures: 400, 600 and 800 °C. The corresponding samples will be further denoted as MFO400, MFO600 and MFO800. Details of the synthesis procedure, structural analysis, as well as various other methods of characterization of these samples have already been published elsewhere [51]. The schematic diagram of the synthesis procedure is given in the Supplementary Information.

The IR reflectivity measurements of the $MgFe_2O_4$ samples in the form of pressed disk-like pellets were carried out at room temperature with a BOMEM DA8 Fourier-transform IR spectrometer. A Hyper beamsplitter and a deuterated triglycine sulfate (DTGS) pyroelectric detector were used to cover the wavenumber region from 90 to 680 cm^{-1}. Micro-Raman spectroscopy was used to estimate the degree of inversion of nanocrystalline $MgFe_2O_4$. Micro-Raman spectra were acquired in the back-scattering configuration using the triple-monochromator Raman system Princeton TriVista 557. Nd:YAG laser line of 532 nm was used as an excitation and the beam was focused onto the samples using 50x objective magnification. Laser power on the sample was 0.08 mW. Raman spectra were deconvoluted using Lorentzian function. More detailed description of infrared and Raman experimental setups is presented in the Supplementary Information.

3. Results and discussion

$MgFe_2O_4$ crystalizes in a cubic spinel structure belonging to the $Fd\bar{3}m$ space group. The full unit cell contains 56 atoms ($Z = 8$), however the smallest Bravais cell, i.e., the primitive cell, has only 14 atoms ($Z = 2$). The factor group analysis for the primitive cell predicts 42 normal modes, three of which are acoustic modes with T_{1u} symmetry, and the remaining 39 Γ-point optical modes are:

$$\Gamma = A_{1g}(R) + E_g(R) + T_{1g} + 3T_{2g}(R) + 2A_{2u} + 2E_u + 4T_{1u}(IR) + 2T_{2u}. \quad (1)$$

Among these modes, four are triply degenerate infrared (IR) modes of T_{1u} symmetry, five are Raman (R) modes, and the remaining modes are silent. Inverse spinels like $NiFe_2O_4$ or $CoFe_2O_4$ show more Raman-active modes than those predicted by factor-group analysis because of inversion of the cations between the tetrahedral and octahedral sites. These spinel structures are characterized by an additional mode in the frequency region where one A_{1g} mode is expected to appear [52,53]. In

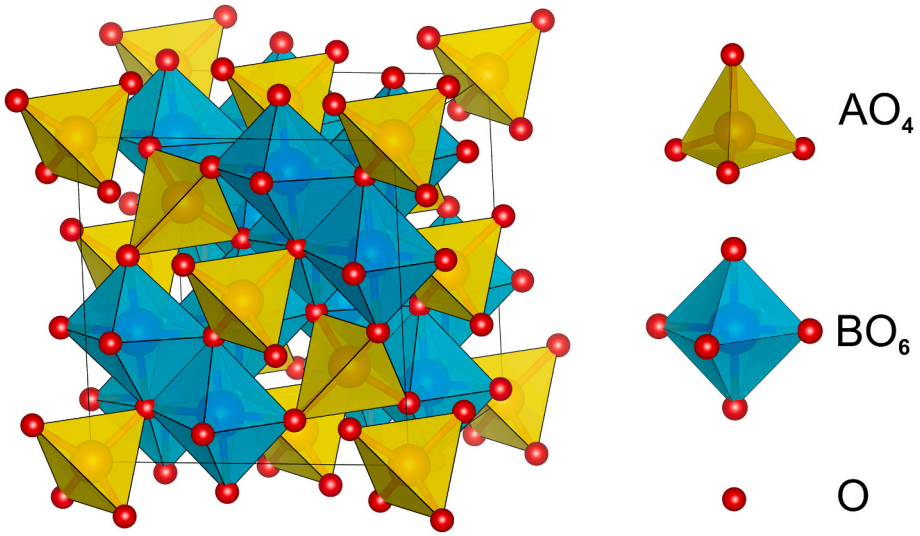

Fig. 1. (Color online) Schematic illustration of normal AB_2O_4 spinel structure with the tetrahedral (AO_4) and octahedral (BO_6) units. The crystal structure visualized by VESTA 3 [50].

the Raman spectra of $MgFe_2O_4$ nanopowders, the A_{1g} mode splits into two modes due to the large difference in mass between Fe^{3+} and Mg^{2+} cations [54–56]. The higher frequency A_{1g} mode corresponds to the vibrations of oxygen anions around Fe^{3+} cations on the tetrahedral sites, whereas the lower frequency mode corresponds to the vibrations of oxygen anions around Mg^{2+} cations on the tetrahedral sites [54,56]. In Fig. 2 are shown deconvoluted room-temperature Raman spectra of MFO400, MFO600 and MFO800 samples, using Lorentzian function. The Raman spectra are presented in the region characteristic for the A_{1g} modes.

Nakagomi et al. [56] have shown that, using corresponding integrated intensities of the two A_{1g} modes, it is possible to quantitatively determine the Mg and Fe content on the tetrahedral sites. Therefore, knowing that the integrated intensities of the two A_{1g} modes are proportional to the concentrations of Mg^{2+} and Fe^{3+} cations on the tetrahedral sites [56], the inversion parameter δ can be calculated from the equation

$$\frac{I\left(A_{1g}^{low}\right)}{I\left(A_{1g}^{high}\right)} = \frac{1-\delta}{\delta} \tag{2}$$

The calculated inversion parameters are 0.52, 0.62 and 0.74 for the MFO400, MFO600 and MFO800 samples, respectively. These data imply that the sample sintered at 400 °C is closer to the normal spinel structure than the sample sintered at 800 °C, which is in complete accordance with the results of positron annihilation analysis of these samples [51]. The inversion parameters obtained from the Raman spectra are also in good agreement with Bloesser et al., who analyzed $MgFe_2O_4$ samples calcined at 400, 600 and 800 °C, and for the sample calcined at 800 °C obtained the inversion degree of 0.72 [18].

The IR reflectivity spectra of $MgFe_2O_4$ nanocrystalline samples are shown in Fig. 3. In the spectra of all samples were found four T_{1u} modes predicted by group theory. Following the seminal work of Waldron [27], most authors label the four T_{1u} modes as ν_1, ν_2, ν_3 and ν_4, indexing them from the highest to the lowest energies. According to Waldron, the highest energy mode ν_1 was attributed to the vibrations of tetrahedra, and the ν_2 mode to the vibrations of octahedra, considering the vibrations of these groups as mostly isolated molecular vibrations [27]. Such conclusions were later also adopted by Hafner [28], and White and DeAngelis [29]. On the other hand, these conclusions were criticized by Preudhomme and Tarte [30–33] as oversimplified. They argued that, in some cases at least, the observed frequencies cannot be assigned to the vibrations of definite coordinated groups (either tetrahedral or octahedral), but instead are related to complex vibrations of the whole spinel lattice. Nevertheless, many authors still rely mostly on the original Waldron's interpretation of these modes [35,38,42–44,57,58]. It is mostly accepted that the two low frequency modes ν_3 and ν_4 originate from complex vibrations involving both tetrahedral and octahedral groups [27,32,33,35–37].

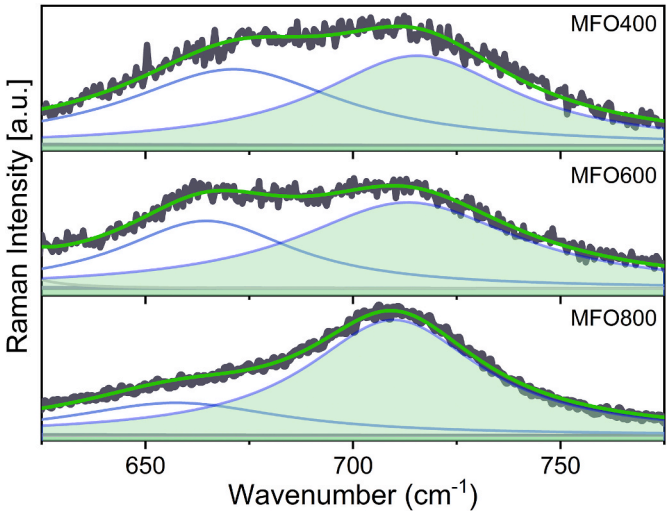

Fig. 2. (Color online) Room-temperature Raman spectra (data in black) of $MgFe_2O_4$ samples sintered at different temperatures, in the region (625–775) cm^{-1}. Experimental curves were deconvoluted with Lorentzian function (blue curves) and cumulative fits are represented by the green curves. The high-frequency A_{1g} mode is shaded for clarity.

The MFO400 sample shows two modes ν_1 and ν_2, centered at around 570 and 405 cm^{-1} respectively. These two modes are present in all spinels. For the MFO600 and MFO800 samples, the third mode ν_3 centered at around 330 cm^{-1} is clearly visible. This mode is present in the MFO400 sample too and appears as an asymmetry of the ν_2 mode. In the IR spectra of some spinels a weak forth mode ν_4 appears around 200 cm^{-1} [28,29,32–36,40,49]. This mode can be observed as a small hump centered at around 210 cm^{-1} in the MFO800 sample spectra, and to a lesser extent also in the MFO600 and MFO400 spectra.

In the low frequency region of the IR spectra in Fig. 3, Drude tail appeared and became more pronounced for the MFO600 and MFO800 samples. Its occurrence in the IR spectra is a clear sign of a presence of free carriers. The presence of free carriers in nanocrystalline $MgFe_2O_4$ comes from the presence of vacancies, which introduce electrons as the majority free carriers, making $MgFe_2O_4$ an n-type semiconductor [59]. When free carriers are present in the material, they can interact with phonons. Since plasmons are longitudinal oscillations, they interact with longitudinal-optical (LO) modes, shifting them towards higher frequencies, whereas the transverse-optical (TO) modes remain unaffected. In the analysis of the reflectivity spectra of $MgFe_2O_4$ nanocrystalline samples, two models, both of which include contribution from free carriers, have been applied to investigate the dielectric response. In both models, the factorized form of dielectric function was used. Compared to the classical oscillator model, this factorized form much better describes phonons in strongly polar ionic crystals, where largely split TO/LO modes can have significantly different dampings [60].

The first model, known in literature as the coupled plasmon-phonon model (CPP) [61,62], presents a direct way to characterize plasmon-phonon coupled modes. In this model, the dielectric function has a form:

$$\varepsilon(\omega) = \varepsilon_\infty \frac{\prod_{j=1}^{m+n} \omega^2 + i\gamma_{LOj}\omega - \omega_{LOj}^2}{\omega^m \prod_{j=1}^{m}(\omega + i\gamma_{Pj}) \prod_{j=1}^{n} \omega^2 + i\gamma_{TOj}\omega - \omega_{TOj}^2}, \tag{3}$$

where ε_∞ is the high frequency dielectric constant, $\omega_{TOj}(\omega_{LOj})$ and $\gamma_{TOj}(\gamma_{LOj})$ are the TO(LO) frequencies and dampings of n phonons ($n = 4$ in our case), which can be coupled with m plasmons with dampings γ_{Pj} ($m = 1$ in our case). From this model, the plasma frequency can be obtained indirectly as [61,62]:

$$\omega_P = \frac{\prod_{j=1}^{n+1} \omega_{LOj}^2}{\prod_{j=1}^{n} \omega_{TOj}^2}, \tag{4}$$

and the frequency of the coupled plasmon-phonon mode is given by [61,62]:

$$\Omega_{LOj} = \sqrt{\omega_{LOj}^2 - \frac{1}{4}\gamma_{LOj}^2}. \tag{5}$$

The second model, named as the decoupled plasmon-phonon (DPP) model, is a conventional additive form for dielectric function of pure phonon and plasmon contributions. This model enables to determine the decoupled phonon and plasma frequencies and dampings using

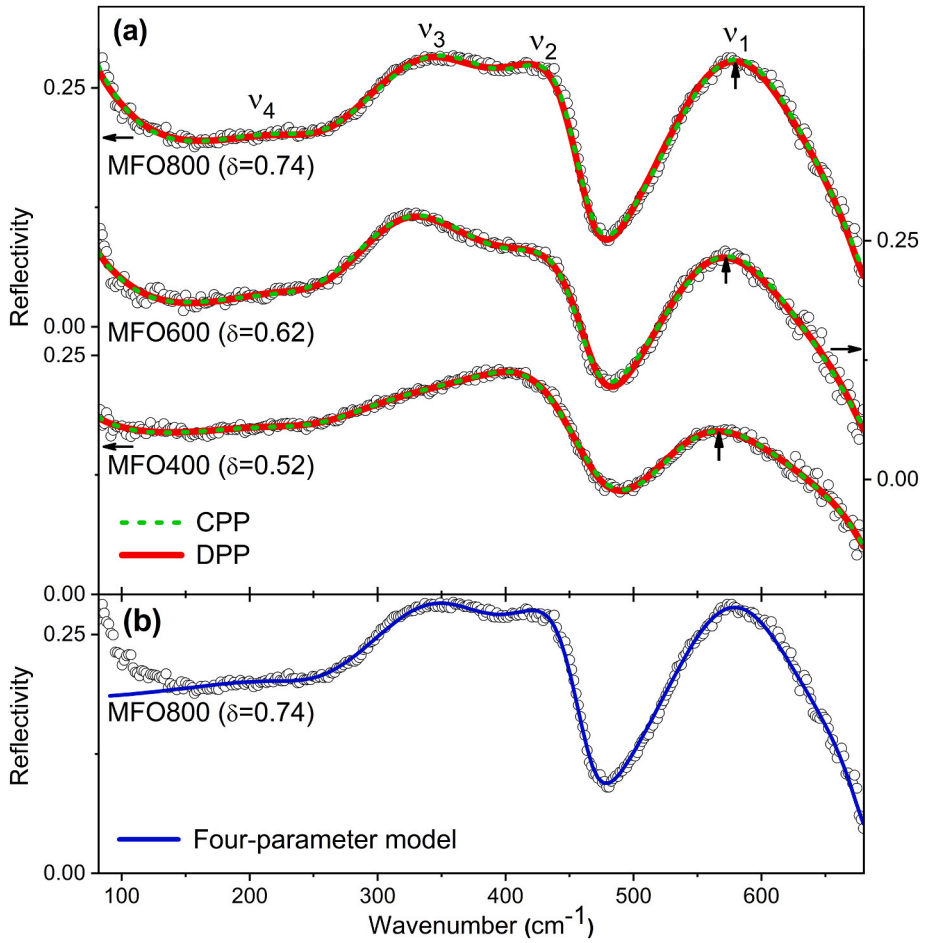

Fig. 3. (Color online) (a) IR reflectivity spectra of $MgFe_2O_4$ nanocrystalline samples sintered at different temperatures together with theoretical fits obtained using the coupled plasmon-phonon (CPP) and decoupled plasmon-phonon (DPP) models. The degree of inversion δ is given in parenthesis. Vertical arrows mark the ν_1 peak (explained in the text). (b) The best fit obtained using the four-parameter model for dielectric function, is also given for the MFO800 sample as an example.

dielectric function in the form [60,63]:

$$\varepsilon\left(\omega\right)=\varepsilon_{\infty}\left(\prod_{j=1}^{n}\frac{\omega_{LOj}^{2}-\omega^{2}-i\gamma_{LOj}\omega}{\omega_{TOj}^{2}-\omega^{2}-i\gamma_{TOj}\omega}-\frac{\omega_{P}^{2}}{\omega(\omega+i\gamma_{P})}\right). \tag{6}$$

The first term in this model represents the phonons contribution, where $\omega_{TOj}(\omega_{LOj})$ and $\gamma_{TOj}(\gamma_{LOj})$ are the TO(LO) frequencies and dampings of phonons. The second term is the Drude term which describes the plasmon mode, where ω_P and γ_P are the frequency and damping of the plasmon mode. In the DPP model, the LO frequencies are actually the frequencies of bare phonons decoupled from plasmon, whereas in the CPP models the LO frequencies are for the coupled plasmon-LO phonon modes. In both models, the TO mode frequencies have the same meaning and are unaffected by free carriers. Without the Drude term, Eq. (6) reduces to the so-called four-parameter model for the dielectric function of phonon spectra [60,63].

In order to properly analyze the IR reflectivity spectra of $MgFe_2O_4$ nanocrystalline samples, the effect of porosity on the IR spectra must be taken into account. In that sense, the Bruggeman effective medium approximation [64,65] is very often used to describe the optical properties of porous nanomaterials. For a homogenous mixture of a material (ε_M) with volume fraction f_M, and air ($\varepsilon = 1$) with fraction (1-f_M), the effective dielectric function ε_{eff} can be obtained from the equation

$$\left(\frac{\varepsilon_{M}-\varepsilon_{eff}}{\varepsilon_{M}+2\varepsilon_{eff}}\right)f_{M}+\left(\frac{1-\varepsilon_{eff}}{1+2\varepsilon_{eff}}\right)(1-f_{M})=0, \tag{7}$$

in which ε_M is described by an appropriate model, in our case by equation (3) or (6). The calculated reflectivity R_{calc} can be obtained using the Fresnel formula

$$R_{calc}=\left|\frac{\sqrt{\varepsilon_{eff}}-1}{\sqrt{\varepsilon_{eff}}+1}\right|^{2}. \tag{8}$$

In the IR spectra fitting procedure, the parameters were automatically tuned until the difference between the experimental (R_{exp}) and calculated (R_{calc}) reflectivity, given by the chi-squared value

$$\chi^{2}=\frac{1}{N}\sum_{i=1}^{N}\left(R_{i,\exp}-R_{i,calc}\right)^{2}, \tag{9}$$

where N is the number of points in spectra, became minimized within the experimental error.

The obtained best fits for both models are shown in Fig. 3(a) (red full and green dashed lines), whereas the best fit parameters are given in Table 1 (CPP model) and Table 2 (DPP model). It can be seen that both models provide satisfactory fits of the experimental spectra. For comparison, the best fit obtained using the four-parameter model for dielectric function, which does not include the free carriers contribution, is also shown in Fig. 3(b) for the MFO800 sample as an example. It is obvious that such a model fails to reproduce experimental spectra at lower frequencies.

Fig. 4 shows the variation of plasma frequency ω_P and damping γ_P for $MgFe_2O_4$ samples sintered at different temperatures, for the both used models. As can be seen, similar behavior of ω_P and γ_P was obtained from the both models. The plasma frequency slightly decreases with sintering

Table 1
Fitting parameters obtained by using the Coupled Plasmon-Phonon (CPP) model, for $MgFe_2O_4$ nanocrystalline samples sintered at different temperatures. Plasma/phonon frequencies and damping values are given in cm^{-1}. The estimated errors are also presented.

Parameters	MFO400	MFO600	MFO800	Est. err.
f_M	0.63	0.7	0.82	±0.02
ω_P	213	200.6	191.1	±5
γ_P	303	188	169	±5
ω_{TO1} (γ_{TO1})	541 (114)	543 (108)	546 (100)	±3 (±5)
ω_{LO1} (γ_{LO1})	684 (48)	679 (45)	677 (50)	±3 (±5)
ω_{TO2} (γ_{TO2})	422 (122)	445 (89)	436 (81)	±5 (±5)
ω_{LO2} (γ_{LO2})	472 (79)	468 (46)	465 (43)	±5 (±5)
ω_{TO3} (γ_{TO3})	321 (192)	317 (123)	338 (131)	±5 (±5)
ω_{LO3} (γ_{LO3})	412 (262)	398 (181)	399 (144)	±5 (±5)
ω_{TO4} (γ_{TO4})	254 (225)	255 (128)	255 (125)	±12 (±12)
ω_{LO4} (γ_{LO4})	266 (166)	256 (98)	258 (99)	±12 (±12)
ω_{LO5} (γ_{LO5})	112 (237)	121 (194)	121 (168)	±5 (±5)

Table 2
Fitting parameters obtained by using the Decoupled Plasmon-Phonon (DPP) model, for $MgFe_2O_4$ nanocrystalline samples sintered at different temperatures. Plasma/phonon frequencies and damping values are given in cm^{-1}. The estimated errors are also presented.

Parameters	MFO400	MFO600	MFO800	Est. err.
f_M	0.62	0.72	0.82	±0.02
ω_P	226	214	194	±5
γ_P	369	231	186	±5
ω_{TO1} (γ_{TO1})	537 (118)	538 (110)	542 (102)	±3 (±5)
ω_{LO1} (γ_{LO1})	663 (36)	663 (47)	662 (47)	±3 (±5)
ω_{TO2} (γ_{TO2})	423 (135)	448 (111)	436 (97)	±5 (±5)
ω_{LO2} (γ_{LO2})	470 (67)	468 (45)	463 (41)	±5 (±5)
ω_{TO3} (γ_{TO3})	323 (204)	315 (111)	332 (122)	±5 (±5)
ω_{LO3} (γ_{LO3})	378 (251)	373 (175)	380 (147)	±5 (±5)
ω_{TO4} (γ_{TO4})	250 (146)	253 (122)	257 (120)	±12 (±12)
ω_{LO4} (γ_{LO4})	252 (125)	256 (99)	258 (98)	±12 (±12)

temperature. On the other hand, the plasma damping decreases significantly for the MFO600 sample, and then further decreases to a lesser extent for the MFO800 sample, resulting in more pronounced Drude tail in the IR spectra of the MFO600 and MFO800 samples. The material volume fraction f_M has increased with increasing sintering temperature (see Tables 1 and 2), indicating that the MFO600 and MFO800 samples became less porous. This is in accordance with previous research on these samples where it was shown that increased sintering temperature leads to larger crystallite sizes and more agglomeration [51]. In samples with larger and more fussed crystallites, with better agglomeration and less pores, the influence of grain boundaries is smaller, having as a consequence the higher electron mobility and longer scattering relaxation time τ. This, in turn, explains the observed significant decrease of plasma dampings, since $\gamma_P = 1/\tau$.

From Tables 1 and 2, it can be seen that in the case of ν_4 mode, the splitting between the TO and LO frequencies is small, meaning that the oscillator strength, being proportional to $(\omega_{LO}^2 - \omega_{TO}^2)$, is also small. The

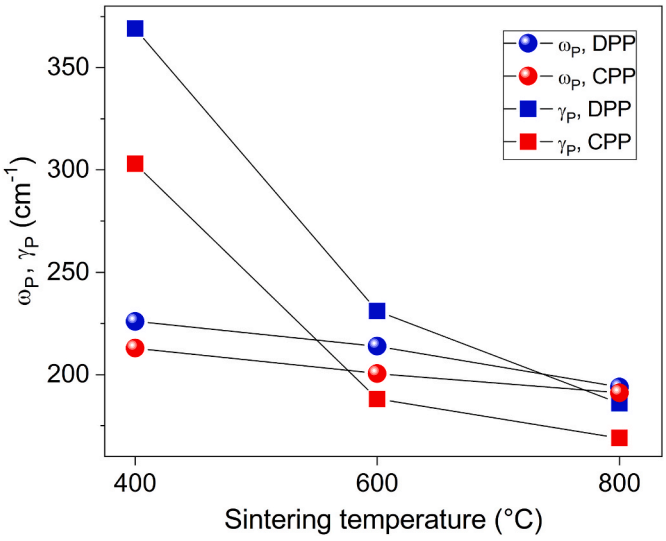

Fig. 4. (Color online) Variation of plasma frequency (ω_P) and damping (γ_P) of $MgFe_2O_4$ nanocrystalline samples sintered at different temperatures, obtained by using the CPP and DPP models.

similar behavior of this mode is found in most other spinels for which this mode is either weak or absent. Other modes exhibit large TO-LO splitting, as common for ionic crystals. The TO frequencies, obtained from both CPP and DPP models, are rather similar for each $MgFe_2O_4$ sample. Such a behavior is expected, as the TO frequencies are not affected by the plasmon-phonon interaction.

In Fig. 5(a) are presented the frequencies of the coupled plasmon-LO phonon modes Ω_{LOj} (obtained from the CPP model, Eq. (3) and Eq. (5)), and the decoupled LO phonon modes ω_{LOj} (from the DPP model, Eq. (6)). It can be seen that for the ν_1 and ν_3 modes, the coupled LO frequencies have higher values than the decoupled ones. The difference between these frequencies is approximately the same for all samples. On the other hand, the coupled/decoupled LO frequencies are quite similar for the ν_2 mode. In the case of ν_4 mode, these frequencies also appear to be similar. However, the ν_4 mode is too weak and broad, whereas the fitting errors are too high, for a definitive conclusion to be drawn. As mentioned before, the LO frequencies obtained from the DPP model are actually the frequencies of bare phonons decoupled from plasmon, whereas the LO frequencies obtained from the CPP model are for the combined plasmon–LO phonon modes. The fact that in the case of ν_1 and ν_3 modes, the LO values obtained by the CPP model are higher than those obtained by the DPP model, implies that these modes are more strongly coupled with free carriers than the ν_2 mode.

The TO frequency behavior for all four IR modes, obtained from the CPP and DPP models (Tables 1 and 2), is presented in Fig. 5(b). In Fig. 3(a), one can notice that the ν_1 peak (marked with vertical arrows), is slightly shifted towards higher frequencies as the sintering temperature and degree of inversion increases, which is also corroborated by the slight increase of ω_{TO1} frequencies obtained from the CPP and DPP models. In the case of $MgFe_2O_4$, the tetrahedral cation-oxygen bonds are of higher force constants and lower bond length than the cation-oxygen octahedral bonds, and the corresponding vibrations of the tetrahedra are of higher frequency [27]. The bonding force between the cation and oxygen also depends on the nature of the cation and its valency [30]. Waldron [27] calculated force constants for some ferrites, and showed for $MgFe_2O_4$ that the force constants of the tetrahedral Fe–O vibrations are higher than the tetrahedral Mg–O vibrations [27]. Therefore, the observed increase of the frequency of the ν_1 mode with the increased degree of inversion is consistent with the tetrahedral origin of this mode, because more Mg^{2+} are replaced with Fe^{3+}. On the other hand, the TO frequency of the ν_2 mode, which mainly originates from the octahedral Fe–O vibrations, shows no consistent shift with the increased sintering

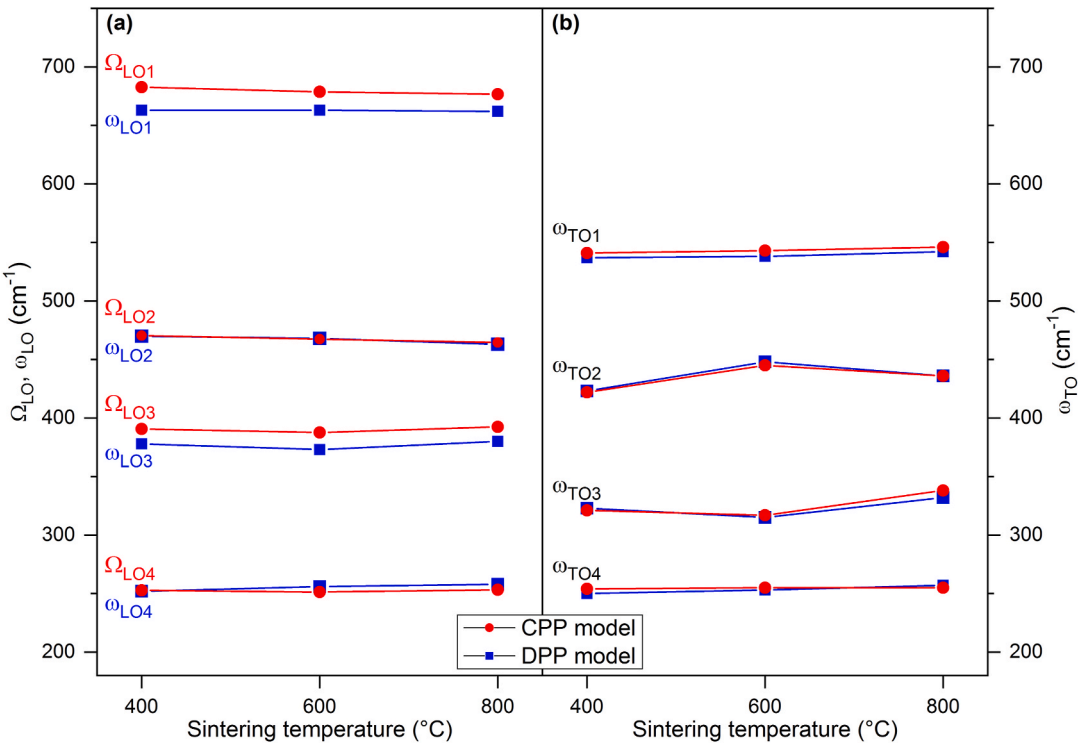

Fig. 5. (Color online) (a) Coupled (Ω_{LOj}) and decoupled (ω_{LOj}) LO phonon frequencies, and (b) the TO phonon frequencies, obtained from the CPP and DPP models, for $MgFe_2O_4$ nanocrystalline samples sintered at different temperatures.

temperature and degree of inversion. It slightly increases for the MFO600 sample, and then slightly decreases for the MFO800 sample. The increase of the TO frequency in the MFO600 sample can be explained by an increasing contribution of the Fe–O tetrahedral vibrations to the ν_2 mode, because with the increasing degree of inversion more Fe^{3+} cations are situated at the tetrahedral sites. With further increase of the degree of inversion (MFO800), one can presume even more complex behavior of the ν_2 mode, where, besides the Fe–O tetrahedral vibrations, the Mg–O octahedral vibrations can participate too. The behavior of the ν_3 mode becomes also more complex with increased

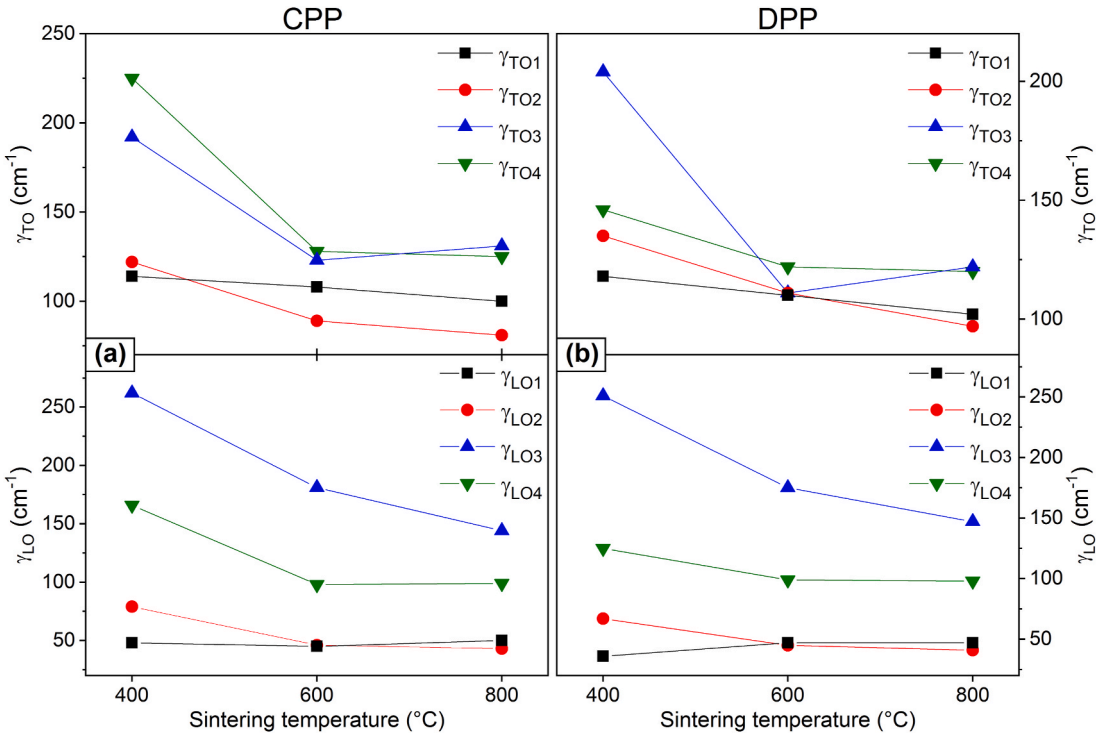

Fig. 6. (Color online) Variation of the TO and LO phonon dampings for $MgFe_2O_4$ nanocrystalline samples sintered at different temperatures, obtained from (a) CPP and (b) DPP models.

degree of inversion. It was already pointed out by Preudhomme and Tarte [31,32] that with higher degree of inversion, coupling between different tetrahedra and octahedra can make infrared vibrations of more complex nature. Consequently, it is no longer realistic to ascribe such vibrations and its frequencies to the localized vibrations of definite coordinated group (tetrahedral or octahedral), but to the vibrations which involve simultaneous participation of different cations (Mg or Fe) and coordinated groups.

The TO and LO phonon dampings obtained from the CPP and DPP models, are shown in Fig. 6. It can be seen that the TO/LO dampings tend to decrease with the increasing sintering temperature. Such a behavior is a consequence of the fact that the increase of sintering temperature produced samples with larger and more fussed crystallites with less pores and smaller influence of grain boundaries. All this in turn can lead to the smaller scattering rates for phonons, which means longer phonon lifetimes and decreased phonon dampings.

From the analysis of the IR spectra based on the CPP and DPP models (Fig. 5(a)), it was obtained that the ν_1 and ν_3 modes are more strongly coupled with free carriers than the ν_2 mode. We propose that this finding may be related to the presence of antisite defects, which are formed in inverse spinels. Namely, when in inverse spinels the trivalent cation replaces the divalent one in tetrahedra, it introduces excess positive charge at this site. Conversely, the octahedral site becomes a site with excess negative charge by introduction of the divalent cation instead of the trivalent one. In inverse $MgFe_2O_4$, positively charged $[Fe^{3+}_{tetra}]^+$ and negatively charged $[Mg^{2+}_{octa}]^-$ antisite defect centers can be formed in tetrahedra and octahedra (presented in Fig. 7), which behave as electron and hole trap centers, respectively [66–68].

If a particular mode has a significant contribution of the Fe–O tetrahedral vibrations, as it is the case for the ν_1 and ν_3 modes, it is quite reasonable to assume that such an infrared mode would be more strongly coupled with free carriers, due to the existence of positively charged $[Fe^{3+}_{tetra}]^+$ antisite defects. In the case of the ν_2 mode, which is mostly of the octahedral origin, the presence of negatively charged $[Mg^{2+}_{octa}]^-$ antisite defects is expected to weaken the plasmon-phonon interaction. With increased degree of inversion, one might expect a stronger plasmon-phonon coupling of the ν_1 and ν_3 modes as more $[Fe^{3+}_{tetra}]^+$ antisite defects should be formed. However, our analysis has shown that the plasmon-phonon coupling strength did not increase with the increased degree of inversion. We suppose that with the increased degree of inversion, when ν_1 and ν_3 vibrations become more complex, a subtle interplay between the tetrahedral Fe–O and octahedral Mg–O vibrations influences the plasmon-phonon coupling, leading to different strength of coupling between particular phonon modes and free carriers. As the exact mechanism of plasmon-phonon coupling in nanosized $MgFe_2O_4$ is not completely clear at the moment, it presents strong motivation for our future research.

4. Conclusions

In summary, we have investigated room-temperature far-IR reflectivity spectra of partially inverse nanocrystalline $MgFe_2O_4$ samples prepared by sol-gel method and sintered at different temperatures (400, 600 and 800 °C). The degree of inversion of $MgFe_2O_4$ samples was estimated from Raman spectra, and was found to increase with the increase of the sintering temperature. The IR spectra exhibited the presence of free carriers (the so-called Drude tail). The plasmon–LO phonon interaction was investigated by using the factorized coupled and decoupled plasmon-phonon models, combined with the Bruggeman effective medium approximation. From the analysis of the IR spectra, the coupled and decoupled phonon frequencies and dampings, as well as plasma frequencies and corresponding dampings of the plasmon mode were obtained. It was shown that with the increased sintering temperature, the phonon and plasmon dampings significantly decreased due to crystallite size increase, smaller porosity, and better connectivity between crystallites. Of particular importance is the finding that the ν_1 and ν_3 modes are more strongly coupled with free carriers than the ν_2 mode. We proposed that in inverse $MgFe_2O_4$ samples, the presence of positively charged $[Fe^{3+}_{tetra}]^+$ and negatively charged $[Mg^{2+}_{octa}]^-$ antisite defects influences the plasmon-phonon interaction. The stronger plasmon-phonon coupling is expected for infrared modes where the contribution of Fe–O tetrahedral vibrations becomes substantial. With the increased degree of inversion, a subtle interplay between the tetrahedral Fe–O and octahedral Mg–O vibrations can lead to different strength of coupling between particular phonon modes and free carriers. Our findings provide a basis for better understanding of plasmon-phonon coupling mechanism in disordered inverse spinels like $MgFe_2O_4$.

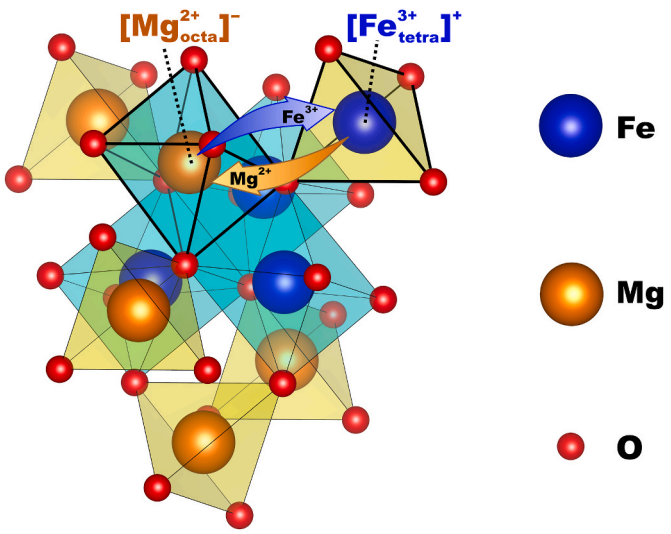

Fig. 7. (Color online) Schematic representation of inversion of trivalent Fe^{3+} and divalent Mg^{2+} cations between octahedra and tetrahedra, and the formation of the $[Fe^{3+}_{tetra}]^+$ and $[Mg^{2+}_{octa}]^-$ antisite defect centers in partially inverse $MgFe_2O_4$. The crystal structure visualized by VESTA 3 [50].

CRediT authorship contribution statement

Novica Paunović: Writing – review & editing, Writing – original draft, Visualization, Software, Methodology, Investigation, Formal analysis, Data curation, Conceptualization. **Zorana Dohčević-Mitrović:** Writing – review & editing, Supervision, Project administration, Methodology, Investigation, Formal analysis, Conceptualization. **Dejan M. Djokić:** Writing – review & editing, Visualization, Project administration, Formal analysis. **Sonja Aškrabić:** Writing – review & editing, Visualization, Investigation, Formal analysis. **Saša Lazović:** Writing – review & editing, Visualization, Investigation. **Ann Rose Abraham:** Writing – review & editing, Resources. **Balakrishnan Raneesh:** Writing – review & editing, Resources. **Nandakumar Kalarikkal:** Writing – review & editing, Project administration, Funding acquisition. **Sabu Thomas:** Writing – review & editing, Supervision.

Declaration of competing interest

The authors declare that they have no known competing financial interests or personal relationships that could have appeared to influence the work reported in this paper.

Data availability

Data will be made available on request.

Acknowledgement

The authors acknowledge funding provided by the Institute of Physics Belgrade, through the grant by the Ministry of Education, Science, and Technological Development of the Republic of Serbia. B. Raneesh acknowledges financial support from the UGC-DAE-Kolkata centre through the CRS project. Parts of the presented research were undertaken through Serbia-India bilateral project (2022–2024, No. 2), within the Program of Cooperation on science and technology between the Ministry of Education, Science and Technological Development of the Republic of Serbia and the Department of Science and Technology of the Ministry of Science and Technology of the Republic of India.

Appendix A. Supplementary data

Supplementary data to this article can be found online at https://doi.org/10.1016/j.mssp.2022.106889.

References

[1] Y.M.Z. Ahmed, E.M.M. Ewais, Z.I. Zaki, In situ synthesis of high density magnetic ferrite spinel ($MgFe_2O_4$) compacts using a mixture of conventional raw materials and waste iron oxide, J. Alloys Compd. 489 (2010) 269–274.
[2] N.M. Deraz, A. Alarifi, Novel preparation and properties of magnesioferrite nanoparticles, J. Anal. Appl. Pyrol. 97 (2012) 55–61.
[3] S.-S. Hong, Catalytic removal of carbon particulates over $MgFe_2O_4$ catalysts, React. Kinet. Catal. Lett. 84 (2005) 311–317.
[4] N. Ma, Y. Yue, W. Hua, Z. Gao, Selective oxidation of styrene over nanosized spinel-type $Mg_xFe_{3-x}O_4$ complex oxide catalysts, Appl. Catal. Gen. 251 (2003) 39–47.
[5] V. Srivastava, Y.C. Sharma, M. Sillanpää, Application of nano-magnesso ferrite (n-$MgFe_2O_4$) for the removal of Co^{2+} ions from synthetic wastewater: kinetic, equilibrium and thermodynamic studies, Appl. Surf. Sci. 338 (2015) 42–54.
[6] D.H.K. Reddy, Y.-S. Yun, Spinel ferrite magnetic adsorbents: alternative future materials for water purification? Coord. Chem. Rev. 315 (2016) 90–111.
[7] R. Dillert, D.H. Taffa, M. Wark, T. Bredow, D.W. Bahnemann, Research Update: photoelectrochemical water splitting and photocatalytic hydrogen production using ferrites (MFe_2O_4) under visible light irradiation, Apl. Mater. 3 (2015), 104001.
[8] G. Takalkar, R.R. Bhosale, F. AlMomani, S. Rashid, R.A. Shakoor, Ni incorporation in $MgFe_2O_4$ for improved CO_2-splitting activity during solar fuel production, J. Mater. Sci. 55 (2020) 11086–11094.
[9] Y. Shimizu, H. Arai, T. Seiyama, Theoretical studies on the impedance-humidity characteristics of ceramic humidity sensors, Sensor. Actuator. 7 (1985) 11–22.
[10] T. Maehara, K. Konishi, T. Kamimori, H. Aono, T. Naohara, H. Kikkawa, Y. Watanabe, K. Kawachi, Heating of ferrite powder by an AC magnetic field for local hyperthermia, Jpn. J. Appl. Phys. 41 (2002) 1620–1621.
[11] K. Konishi, T. Maehara, T. Kamimori, H. Aono, T. Naohara, H. Kikkawa, Y. Watanabe, K. Kawachi, Heating ferrite powder with AC magnetic field for thermal coagulation therapy, J. Magn. Magn Mater. 272–276 (2004) 2428–2429.
[12] S. Kanagesan, M. Hashim, S. Tamilselvan, N.B. Alitheen, I. Ismail, G. Bahmanrokh, Cytotoxic effect of nanocrystalline $MgFe_2O_4$ particles for cancer cure, J. Nanomater. (2013), 865024, 2013.
[13] F. Foroughi, S.A. Hassanzadeh-Tabrizi, A. Bigham, In situ microemulsion synthesis of hydroxyapatite-$MgFe_2O_4$ nanocomposite as a magnetic drug delivery system, Mater. Sci. Eng. C 68 (2016) 774–779.
[14] Q. Chen, Z.J. Zhang, Size-dependent superparamagnetic properties of $MgFe_2O_4$ spinel ferrite nanocrystallites, Appl. Phys. Lett. 73 (1998) 3156–3158.
[15] N. Sivakumar, S.R.P. Gnanakan, K. Karthikeyan, S. Amaresh, W.S. Yoon, G.J. Park, Y.S. Lee, Nanostructured $MgFe_2O_4$ as anode materials for lithium-ion batteries, J. Alloys Compd. 509 (2011) 7038–7041.
[16] Y. Yin, N. Huo, W. Liu, Z. Shi, Q. Wang, Y. Ding, J. Zhang, S. Yang, Hollow spheres of $MgFe_2O_4$ as anode material for lithium-ion batteries, Scripta Mater. 110 (2016) 92–95.
[17] Y. Pan, Y. Zhang, X. Wei, C. Yuan, J. Yin, D. Cao, G. Wang, $MgFe_2O_4$ nanoparticles as anode materials for lithium-ion batteries, Electrochim. Acta 109 (2013) 89–94.
[18] A. Bloesser, H. Kurz, J. Timm, F. Wittkamp, C. Simon, S. Hayama, B. Weber, U.-P. Apfel, R. Marschall, Tailoring the size, inversion parameter, and absorption of phase-pure magnetic $MgFe_2O_4$ nanoparticles for photocatalytic degradations, ACS Appl. Nano Mater. 3 (2020) 11587–11599.
[19] L. Zheng, K. Fang, M. Zhang, Z. Nan, L. Zhao, D. Zhou, M. Zhu, W. Li, Tuning of spinel magnesium ferrite nanoparticles with enhanced magnetic properties, RSC Adv. 8 (2018) 39177–39181.
[20] N. Sivakumar, A. Narayanasamy, J.M. Greneche, R. Murugaraj, Y.S. Lee, Electrical and magnetic behaviour of nanostructured $MgFe_2O_4$ spinel ferrite, J. Alloys Compd. 504 (2010) 395–402.
[21] M. Radović, Z. Dohčević-Mitrović, N. Paunović, S. Bošković, N. Tomić, N. Tadić, I. Belča, Infrared study of plasmon–phonon coupling in pure and Nd-doped CeO_{2-y} nanocrystals, J. Phys. Appl. Phys. 48 (2015), 065301.
[22] Z.V. Popović, M. Grujić-Brojčin, N. Paunović, M.M. Radonjić, V.D. Araújo, M.I. B. Bernardi, M.M. de Lima, A. Cantarero, Far-infrared spectroscopic study of CeO_2 nanocrystals, J. Nanoparticle Res. 17 (2015) 23.
[23] J. Mitric, N. Paunovic, M. Mitric, B. Vasic, U. Ralevic, J. Trajic, M. Romcevic, W. D. Dobrowolski, I.S. Yahia, N. Romcevic, Surface optical phonon – plasmon interaction in nanodimensional CdTe thin films, Phys. E Low-dimens. Syst. Nanostruct. 104 (2018) 64–70.
[24] X. Zhou, L. Liu, J. Sun, N. Zhang, H. Sun, H. Wu, W. Tao, Effects of $(Mg_{1/3}Sb_{2/3})^{4+}$ substitution on the structure and microwave dielectric properties of $Ce_2Zr_3(MoO_4)_9$ ceramics, Journal of Advanced Ceramics 10 (2021) 778–789.
[25] H. Tian, J. Zheng, L. Liu, H. Wu, H. Kimura, Y. Lu, Z. Yue, Structure characteristics and microwave dielectric properties of $Pr_2(Zr_{1-x}Ti_x)_3(MoO_4)_9$ solid solution ceramic with a stable temperature coefficient, J. Mater. Sci. Technol. 116 (2022) 121–129.
[26] L. Huang, Z.F. Li, P.P. Chen, Y.H. Zhang, W. Lu, Far infrared reflection spectra of $InAs_xSb_{1-x}$ (x = 0-0.4) thin films, J. Appl. Phys. 113 (2013), 213112.
[27] R.D. Waldron, Infrared spectra of ferrites, Phys. Rev. 99 (1955) 1727–1735.
[28] S. Hafner, Ordnung/Unordnung und Ultrarotabsorption IV. Die Absorption einiger Metalloxyde mit Spinellstruktur, Z. für Kristallogr. - Cryst. Mater. 115 (1961) 331–358.
[29] W.B. White, B.A. DeAngelis, Interpretation of the vibrational spectra of spinels, Spectrochim. Acta Mol. Spectros 23 (1967) 985–995.
[30] J. Preudhomme, P. Tarte, Infrared studies of spinels–I: a critical discussion of the actual interpretations, Spectrochim. Acta Mol. Spectros 27 (1971) 961–968.
[31] J. Preudhomme, P. Tarte, Infrared studies of spinels–II: the experimental bases for solving the assignment problem, Spectrochim. Acta Mol. Spectros 27 (1971) 845–851.
[32] J. Preudhomme, P. Tarte, Infrared studies of spinels–III: the normal II–III spinels, Spectrochim. Acta Mol. Spectros 27 (1971) 1817–1835.
[33] J. Preudhomme, P. Tarte, Infrared studies of spinels–IV: normal spinels with a high-valency tetrahedral cation, Spectrochim. Acta Mol. Spectros 28 (1972) 69–79.
[34] P. Thibaudeau, F. Gervais, Ab initioinvestigation of phonon modes in the $MgAl_2O_4$ spinel, J. Phys. Condens. Matter 14 (2002) 3543–3552.
[35] O.S. Josyulu, J. Sobhanadri, The far-infrared spectra of some mixed cobalt zinc and magnesium zinc ferrites, Phys. Status Solidi 65 (1981) 479–483.
[36] Z.V. Marinković Stanojević, N. Romčević, B. Stojanović, Spectroscopic study of spinel $ZnCr_2O_4$ obtained from mechanically activated ZnO–Cr_2O_3 mixtures, J. Eur. Ceram. Soc. 27 (2007) 903–907.
[37] M. Lenglet, F. Hochu, Correlation between ionic-covalent parameters and infrared spectroscopic data in II-III transition metal spinel-type oxides, Mater. Res. Bull. 32 (1997) 863–872.
[38] A. Pradeep, P. Priyadharsini, G. Chandrasekaran, Sol–gel route of synthesis of nanoparticles of $MgFe_2O_4$ and XRD, FTIR and VSM study, J. Magn. Magn Mater. 320 (2008) 2774–2779.
[39] N.W. Grimes, A.J. Collett, Correlation of infra-red spectra with structural distortions in the spinel series $Mg(Cr_xAl_{2-x})O_4$, Phys. Status Solidi 43 (1971) 591–599.
[40] V.A.M. Brabers, Ionic ordering and infrared spectra of some II-IV spinels, Phys. Status Solidi 12 (1972) 629–636.
[41] M.E. Striefler, G.R. Barsch, S.-I. Akimoto, Infrared absorption spectra of the spinels Fe_2SiO_4 and Co_2SiO_4, Spectrochim. Acta Mol. Spectros 36 (1980) 275–278.
[42] K.A. Mohammed, A.D. Al-Rawas, A.M. Gismelseed, A. Sellai, H.M. Widatallah, A. Yousif, M.E. Elzain, M. Shongwe, Infrared and structural studies of Mg1–xZnxFe2O4 ferrites, Phys. B Condens. Matter 407 (2012) 795–804.
[43] H. Dawoud, L.S.A. Ouda, S. Shaat, FT-IR studies of nickel substituted polycrystalline zinc spinel ferrites for structural and vibrational investigations, Chemical Science Transactions 8 (2017) 179–188.
[44] A. Pradeep, G. Chandrasekaran, FTIR study of Ni, Cu and Zn substituted nano-particles of $MgFe_2O_4$, Mater. Lett. 60 (2006) 371–374.
[45] Z.V. Popović, G. De Marzi, M.J. Konstantinović, A. Cantarero, Z. Dohčević-Mitrović, M. Isobe, Y. Ueda, Phonon properties of the spinel oxide $MgTi_2O_4$ with the S=1/2 pyrochlore lattice, Phys. Rev. B 68 (2003), 224302.
[46] Z.Ž. Lazarević, Č. Jovalekić, A. Rečnik, V.N. Ivanovski, A. Milutinović, M. Romčević, M.B. Pavlović, B. Cekić, N.Ž. Romčević, Preparation and characterization of spinel nickel ferrite obtained by the soft mechanochemically assisted synthesis, Mater. Res. Bull. 48 (2013) 404–415.
[47] Z.V. Marinković Stanojević, N. Romčević, B. Stojanović, Spectroscopic study of spinel ZnCr2O4 obtained from mechanically activated ZnO–Cr2O3 mixtures, J. Eur. Ceram. Soc. 27 (2007) 903–907.
[48] E.Z. Katsnelson, A.G. Karoza, L.A. Meleshchenko, L.A. Bashkirov, IR reflection spectra of manganese-zinc ferrites, Phys. Status Solidi 152 (1989) 657–666.
[49] H.D. Lutz, B. Müller, H.J. Steiner, Lattice vibration spectra. LIX. Single crystal infrared and Raman studies of spinel type oxides, J. Solid State Chem. 90 (1991) 54–60.
[50] K. Momma, F. Izumi, VESTA 3 for three-dimensional visualization of crystal, volumetric and morphology data, J. Appl. Crystallogr. 44 (2011) 1272–1276.
[51] A.R. Abraham, B. Raneesh, P.M.G. Nambissan, D. Sanyal, S. Thomas, N. Kalarikkal, Defects characterisation and studies of structural properties of sol–gel synthesised $MgFe_2O_4$ nanocrystals through positron annihilation and supportive spectroscopic methods, Phil. Mag. 100 (2020) 32–61.
[52] V.G. Ivanov, M.V. Abrashev, M.N. Iliev, M.M. Gospodinov, J. Meen, M.I. Aroyo, Short-range B-site ordering in the inverse spinel ferrite $NiFe_2O_4$, Phys. Rev. B 82 (2010), 024104.
[53] P. Chandramohan, M.P. Srinivasan, S. Velmurugan, S.V. Narasimhan, Cation distribution and particle size effect on Raman spectrum of $CoFe_2O_4$, J. Solid State Chem. 184 (2011) 89–96.

[54] V. D'Ippolito, G.B. Andreozzi, D. Bersani, P.P. Lottici, Raman fingerprint of chromate, aluminate and ferrite spinels, J. Raman Spectrosc. 46 (2015) 1255–1264.
[55] B.D. Hosterman, Raman Spectroscopic Study of Solid Solution Spinel Oxides, University of Nevada, Las Vegas, 2011.
[56] F. Nakagomi, S.W. da Silva, V.K. Garg, A.C. Oliveira, P.C. Morais, A. Franco, Influence of the Mg-content on the cation distribution in cubic $Mg_xFe_{3-x}O_4$ nanoparticles, J. Solid State Chem. 182 (2009) 2423–2429.
[57] A. Sankaramahalingam, J.B. Lawrence, Structural, optical, and magnetic properties of $MgFe_2O_4$ synthesized with addition of copper, synthesis and reactivity in inorganic, metal-organic, Nano-Metal Chemistry 42 (2012) 121–127.
[58] Z.Ž. Lazarević, Č. Jovalekić, V.N. Ivanovski, A. Rečnik, A. Milutinović, B. Cekić, N.Ž. Romčević, Characterization of partially inverse spinel $ZnFe_2O_4$ with high saturation magnetization synthesized via soft mechanochemically assisted route, J. Phys. Chem. Solid. 75 (2014) 869–877.
[59] J. Guo, L. Shi, L. Wu, S. Pan, X. Yuan, J. Zhao, Spin-polarized electron transport in highly reduced $MgFe_2O_{4-\delta}$, Mater. Res. Express 5 (2018), 126301.
[60] F. Gervais, High-temperature infrared reflectivity spectroscopy by scanning interferometry, in: K.J. Button (Ed.), Infrared and Millimeter Waves, Academic Press, New York, 1983, pp. 279–339.
[61] A.A. Kukharskii, Plasmon-phonon coupling in GaAs, Solid State Commun. 13 (1973) 1761–1765.
[62] O.K. Kim, W.G. Spitzer, Study of plasmon–LO-phonon coupling in Te-doped $Ga_{1-x}Al_xAs$, Phys. Rev. B 20 (1979) 3258–3266.
[63] F. Gervais, Optical conductivity of oxides, Mater. Sci. Eng. R Rep. 39 (2002) 29–92.
[64] D.A.G. Bruggeman, Berechnung verschiedener physikalischer Konstanten von heterogenen Substanzen. I. Dielektrizitätskonstanten und Leitfähigkeiten der Mischkörper aus isotropen Substanzen, Ann. Phys. 416 (1935) 636–664.
[65] J.E. Spanier, I.P. Herman, Use of hybrid phenomenological and statistical effective-medium theories of dielectric functions to model the infrared reflectance of porous SiC films, Phys. Rev. B 61 (2000) 10437–10450.
[66] T.A. Bazilevskaya, V.T. Gritsyna, D.V. Orlinski, L.V. Udalova, A.V. Voitsenya, The effect of composition, processing conditions, and irradiation, on lattice defects in spinel ceramics, J. Nucl. Mater. 253 (1998) 133–140.
[67] N. Pathak, B. Sanyal, S.K. Gupta, R.M. Kadam, $MgAl_2O_4$ both as short and long persistent phosphor material: role of antisite defect centers in determining the decay kinetics, Solid State Sci. 88 (2019) 13–19.
[68] N. Matsubara, T. Masese, E. Suard, O.K. Forslund, E. Nocerino, R. Palm, Z. Guguchia, D. Andreica, A. Hardut, M. Ishikado, K. Papadopoulos, Y. Sassa, M. Månsson, Cation distributions and magnetic properties of ferrispinel $MgFeMnO_4$, Inorg. Chem. 59 (2020) 17970–17980.